Journal of the European Ceramic Society 45 (2025) 117651

Contents lists available at ScienceDirect

Journal of the European Ceramic Society

journal homepage: www.elsevier.com/locate/jeurceramsoc

Additive manufacturing of scaffolds from porous glass microspheres via masked stereolithography: Printing challenges and sustainable applications

Mokhtar Mahmoud [a,b], Hamada Elsayed [b,*], Jozef Kraxner [a], Martin Michálek [a], Beáta Pecušová [a], Montaha Anjass [c,d], Nikhil Arya [d], Enrico Bernardo [b], Dušan Galusek [a]

[a] FunGlass, Alexander Dubček University of Trenčín, Trenčín 91150, Slovakia
[b] Department of Industrial Engineering, University of Padova, Padova 35131, Italy
[c] Department of Chemistry, University of Sharjah, Sharjah 27272, United Arab Emirates
[d] Institute of Inorganic Chemistry I, Ulm University, Albert-Einstein-Allee 11, Ulm 89081, Germany

ARTICLE INFO

Keywords:
Additive manufacturing
Waste glasses
Porous glass microsphere
Photocatalytic applications
Masked stereolithography

ABSTRACT

Additive manufacturing techniques, particularly masked stereolithography (MSLA), enable the creation of intricate and precise porous glass structures. However, preserving slurry stability remains a significant challenge for MSLA. For the first time, this study offers a novel approach to printing highly porous glass microspheres by addressing particle aggregation and sedimentation issues. Particle settling and separation are effectively avoided by coating the porous glass microspheres with polyethylene glycol (PEG) before combining them with photocurable resin. Using this approach, scaffolds with a diamond-shaped cellular structure and 90 % open porosity were fabricated via MSLA. Furthermore, incorporating 7.5 wt% titania nanoparticles enabled the fabrication of 3D composite structures with photocatalytic activity. The printed scaffolds, consisting of pure porous glass microspheres and porous glass microspheres containing titania, were assessed for their capacity to adsorb and photodegrade methylene blue dye. The addition of titania nanoparticles significantly enhanced photocatalytic performance, increasing dye remediation efficiency from 74 % to 100 %. The findings demonstrate the ability of 3D printing technology to repurpose and improve the usefulness of discarded glass, providing a sustainable and effective method for addressing a variety of environmental issues.

1. Introduction

Significant environmental issues have emerged related to the improper disposal and inefficient recycling of various materials, including glass waste [1–3]. The non-biodegradable nature of glass contributes to its accumulation in landfills, where it depletes vital resources and obstructs available space [4]. In regions where landfill capacity is inadequate, and waste management systems are ineffective, waste disposal and emissions emerge as significant obstacles [5]. Simultaneously, there has been a substantial surge in water contamination due to micropollutants, which poses substantial hazards to both ecological health and human progress. This has increased the demand for cost-effective and environmentally friendly water treatment methods to comply with water quality regulations; consequently, novel approaches are required. The efficacy of porous glass filtration systems in eliminating hazardous contaminants and colored compounds has been the subject of numerous studies [6,7]. One of the solutions that overcomes the difficulties related to discarded glasses and at the same time, provides a tool for wastewater remediation is the development and use of porous glass microspheres [5]. This required finding of a novel method for printing highly porous structures using porous glass microspheres. In the present work, flame synthesis can be used to create porous glass microspheres from alkali-activated fiberglass waste, which can then be 3D printed using MSLA with and without added TiO_2 nanoparticles. Following the debinding procedure, the printed structures can be partially sintered to construct functional 3D porous structures with the required strength and to fabricate structures with desired photocatalytic additives.

Heterogeneous photocatalysis utilizing materials such as TiO_2 has demonstrated significant potential in the degradation of hazardous pigments and contaminants [8–10]. Dye adsorption on the surface of the photocatalyst is a critical preliminary phase in the photodegradation process, which is a complex interplay of numerous elements. Adsorption, an essential condition for photodegradation, exerts an influence on

* Corresponding author.
E-mail address: hamada.elsayed@unipd.it (H. Elsayed).

https://doi.org/10.1016/j.jeurceramsoc.2025.117651
Received 10 April 2025; Received in revised form 3 July 2025; Accepted 4 July 2025
Available online 5 July 2025

the entire process efficiency and efficacy. The degree of dye adsorption on the titania surface dictates the availability of dye molecules for photodegradation; consequently, this parameter has a substantial influence on the degradation overall efficacy. In this context, the porosity of the substrate is crucial for enhanced adsorption and, by extension, photodegradation of organic pigments [11,12]. Porous substrates possess a greater specific surface area and active sites, which facilitates the adsorption of a larger number of dye molecules [13]. The presence of these active sites on porous substrates facilitates more effective interactions between dye molecules and the photocatalyst surface, hence enhancing the possibility of successful photodegradation [14]. Increased porosity directly correlates with enhanced degradation efficiency, making it a vital consideration in the development of efficient photocatalytic systems [15,16].

Heterogeneous photocatalyst systems with 3D porous structures provide exciting options by providing required mechanical strength and stability to active materials [17]. 3D printing, especially MSLA is capable of creating complex and accurate porous glass structures, allowing for mass customization and waste reduction [18]. However, MSLA systems face significant challenges owing to inherent slurry stability concerns. These impede the production of high-quality porous glass products, compromising their structural integrity and performance. Slurry instability, inadequate resin absorption, segregation, poor dispersion, material waste, and post-processing problems are among the most significant obstacles to the process [16,19,20].

Segregation within the slurry exacerbates these difficulties since resin absorption causes concentration gradients, resulting in changes in material characteristics throughout the printed item [21]. As a result, establishing structural regularity and constant performance becomes more challenging. Insufficient material dispersion within the slurry creates another barrier, impeding the printing process and resulting in faults in the finished product. The clumping of particles and uneven layering during printing impair porosity control, affecting the mechanical characteristics and surface quality of printed ceramics [21]. Inefficiencies caused by slurry instability and resin absorption not only slow down the manufacturing process but also lead to material waste. Printing faulty components or discarding unsuccessful prints owing to these issues raises manufacturing costs and reduces overall efficiency. Furthermore, the complexity includes post-processing operations like drying, debinding, and sintering, which are required to achieve the desirable characteristics in porous ceramics. Difficulties associated with printing, including irregular resin absorption and segregation, confound these processes and impede the achievement of the desired porosity and strength [21].

To overcome these numerous limitations, substantial progress will be required in material composition, printing techniques, and process parameters. Researchers perpetually strive for innovative advancements to construct superior porous ceramic products via MSLA utilizing controlling resin absorption, enhancing slurry stability, and optimizing printing parameters [22].

This work provides a novel approach for printing highly porous glass microspheres using MSLA. The application of polyethylene glycol (PEG) coating to porous materials before combining them with a photosensitive resin is proposed to prevent particle settling or separation. The addition of PEG was crucial for the homogeneous printing of waste glass-derived microspheres, both with and without TiO_2 nanoparticles. The PEG coating played a key role in mitigating the segregation issues typically encountered with porous microspheres. Partial sintering after debinding resulted in highly porous 3D structures [22].

In addition, the work attempts to reduce the use of natural resources in glass manufacturing while also extending the lifetime of waste glass via recovery and upcycling. The investigation of waste glass as a sustainable medium for wastewater treatment, in conjunction with 3D printing and photocatalytic technology, offers an innovative and ecologically responsible approach to tackling environmental issues while promoting a circular economy. The results of this study might pave the way for more efficient and cost-effective water treatment technologies, resulting in a cleaner, greener future.

2. Materials and methods

The chemical composition of the starting material (fiberglass waste received from Johns Manville Slovakia, a.s.- Trnava), provided in Table 1, was determined by the Bruker Tiger S8 X-ray fluorescence spectrometer (WDXRF). The waste fiberglass was crushed and sieved through a 40 μm analytical sieve. It was then alkali-activated in a 9 M KOH solution, as described previously [23]. After curing at 75°C, the gel was crushed and sieved again using analytical sieves to yield a 40–80 μm fraction. The precursor material generated by alkali activation was fed into an oxygen-methane torch using a vacuum powder feeder with oxygen as a carrier gas. The precursor powder melted in the flame, yielding micrometer-sized droplets of glass melt, which were then quenched with deionized water, yielding porous glass microspheres (PGM) with the composition outlined in Table 1. PGMs were isolated by microfiltration through a ceramic filter with a pore size of less than 0.3 μm.

The PGMs were manually mixed for 15 min with PEG solution (Sigma-Aldrich, Germany) at 7 wt% related to PGMs weight, then dried at room temperature for 24 h. The dried PGMs coated with PEG were homogenized at 2000 rpm for 10 min in a commercially available photocurable resin (Prusament Resin Flex80 Transparent) with a solid loading content of 50 wt%. The rheological behavior of the suspension was analyzed using a rotational rheometer (Rheometer-Viscometer Haake Mars III) with a plate-on-plate setup, applying shear rates ranging from 1 to 2000 s^{-1} and from 1 to 50 s^{-1} . The measurements were conducted at 25°C.

The Glass microspheres slurries were printed by MSLA (Prusa SL1S, Prusa Research a.s., Prague, Czech Republic). The steps mentioned above were also replicated to print PGMs with TiO_2. In this case, PGMs coated with PEG were mixed with 7.5 wt% of TiO_2 (21 nm, Evonik Degussa GmbH, Germany). The resulting mixture was then homogenized with photocurable resin at a speed of 2000 rpm for 10 min. This combination is referred to as PGMs+TiO_2.

The printer operated in the visible light range between 400 and 500 nm, with a layer thickness of 50 μm. The exposure duration for each layer was 4 s. The curing depth data is provided in Figure S1. The intersecting layers were designed to create diamond-shaped cell scaffolds with a porosity of 90 %. They were prepared in the form of cubic blocks, measuring roughly 13 mm × 13 mm × 13 mm. The geometrical models (STL, Standard Triangulation Language) were obtained through preliminary computational studies using the Rhinoceros 6 program package (Robert McNeel & Associates, Seattle, WA, USA).

Following a de-binding process under air condition at 330 °C for 12 h (heating rate 0.3 °C/min) and subsequent heating at 600 °C for 5 h (heating rate 0.5 °C/min), the printed green objects were fired at 1000 °C (heating rate 10 °C/min) for 1 h. The thermal profiles of porous glass microspheres and photocurable resin are presented in Figure S2. The analyses were performed using a Netzsch TMA 402 F1 Hyperion. A non-photocurable liquid silicone polymer (H62C, Wacker-Chemie GmbH, Munich, Germany) was blended with a commercial photocurable resin as a preceramic polymer binder to enhance bonding among constituent PGMs. Silicone binder (5 wt% with respect to photocurable resin) was added to the previous formulation (PGMs+TiO_2), replacing the resin, and termed PGMs+TiO_2+Si.

The geometric density was evaluated by considering the mass to volume ratio. The apparent and true densities were measured by a helium pycnometer (Anton Paar, Ultrapyc 3000), operating on bulk or finely crushed samples, respectively. The total porosity (P) was also determined. The compressive strength of the fired objects was measured using a universal testing machine (Quasar 25, Galdabini S.p.a., Cardano al Campo, Italy), operating at a crosshead speed of 0.5 mm/min.

X-ray diffraction (XRD) analysis was conducted on the samples before and after sintering to detect any crystallized phases. The analysis

Table 1
Chemical composition of the investigated glass waste and porous glass microspheres in wt%.

Oxides	SiO_2	CaO	Al_2O_3	B_2O_3	Na_2O	K_2O	MgO	Fe_2O_3	TiO_2
Fiber glass waste	56.40 ± 0.60	23.20 ± 0.08	13.60 ± 0.20	5.10 ± 0.02	0.40 ± 0.05	0.60 ± 0.02	0.10 ± 0.01	0.40 ± 0.01	0.20 ± 0.03
Porous Glass Microspheres	59 ± 2	19.6 ± 0.9	11.6 ± 0.9	1.8 ± 0.1	0.30 ± 0.02	5.9 ± 0.1	1.1 ± 0.1	0.30 ± 0.02	0.40 ± 0.01

was carried out using powder diffractometer Panalytical Empyrean, with Cu Kα radiation (λ=1.5405 Å) and a 2Θ range of 10–70°. The microstructure of the printed PGMs samples was examined before and after sintering using scanning electron microscopy (SEM, Jeol JSM 7600 F, Tokyo, Japan) at an accelerating voltage of 1.2 kV. Structural and surface modifications induced by the sintering process of 3D printed PGMs were detected using Atomic Force Microscopy (AFM), Bruker's Dimension XR scanning probe microscope (Innova SPM), and the 3D surface topography and roughness were determined. The imaging of surface topography was performed in tapping mode using an antimony (n) doped silicon probe (Model: NCHV-A, 0.01–0.025 Bruker AFM Probes) with a scan rate of 0.50 Hz. The measurement area for the sample was 3 × 3 μm. The topography images were line-by-line leveled and corrected for better depiction; for data evaluation, a slope correction was applied using the software Nanoscope Analysis 1.50. The Nanoscope software performed the 3D topography and cross-section selection to define the roughness profile.

The fabricated PGMs and PGMs containing TiO_2 objects of the same weight (0.3 g) were submerged for 75–120 min in 50 mL of methylene blue solution at an initial concentration of 50 mg/L to study their adsorption and degradation capacities. The degradation tests included exposing the test to UV light and measuring the solution's absorbance at 664 nm (λmax) using a UV–VIS spectrophotometer (Jasco V-650, USA) to estimate the residual dye concentration.

3. Results and discussion

Generating slurries with a high solid loading, low viscosity, and good dispersibility is a key challenge in the 3D printing of MSLA-based ceramic [24,25]. Generally, dense ceramic parts can be obtained at solid loadings above 40 vol% and slurry viscosities below 3000 mPa·s, meeting the requirements of typical MSLA equipment. Viscosity reflects the fluidity of the slurry and affects the slurry's residential time in the resin tank. The shorter the time, the higher the printing efficiency and shape accuracy of MSLA. Homogeneous dispersion of PGMs within photo-sensitive resin is crucial for successful 3D printing, as uneven distribution can lead to printing failures due to poor material integrity [26]. The porous structure of PGMs poses a challenge, often causing segregation after conventional mixing and resulting in a lack of homogeneity within the resin matrix, see Fig. 1.

The PGMs coated with PEG showed uniform distribution within the resin. The coating process was crucial in mitigating the segregation issues typically encountered with PGMs. PEG, known for its excellent wetting properties and ability to enhance particle dispersion, worked as an effective dispersing agent [26]. The schematic diagram (Fig. 1) illustrates the effectiveness of the proposed approach in homogeneously dispersing the PGMs within the resin. The even distribution of PGMs throughout the resin matrix demonstrates the efficacy of the PEG coating method in overcoming the challenges posed by the porous structure of PGMs. As a result of the optimized dispersion technique, the printing process proceeded smoothly and efficiently. The uniform distribution of PGMs within the resin matrix contributed to improved material consistency and printing quality, ultimately leading to the successful fabrication of the desired 3D structures.

Preliminary experiments demonstrated that using our novel approach prevented the segregation caused by direct mixing of PEG with resin [27] or even dispersing the PGMs in the resin without any additives, as schematically shown in Fig. 1. A distinctly different shear rate dependencies of viscosity were observed for slurries prepared using various approaches. While smaller variation in viscosity was found starting from a shear rate of 400 s^{-1} , all slurries exhibited rheological behaviour characteristic of non-Newtonian fluids. Shear-thinning behavior was observed for slurries containing coated PGMs with PEG, in which the viscosity decreased with an increase in shear rate, as

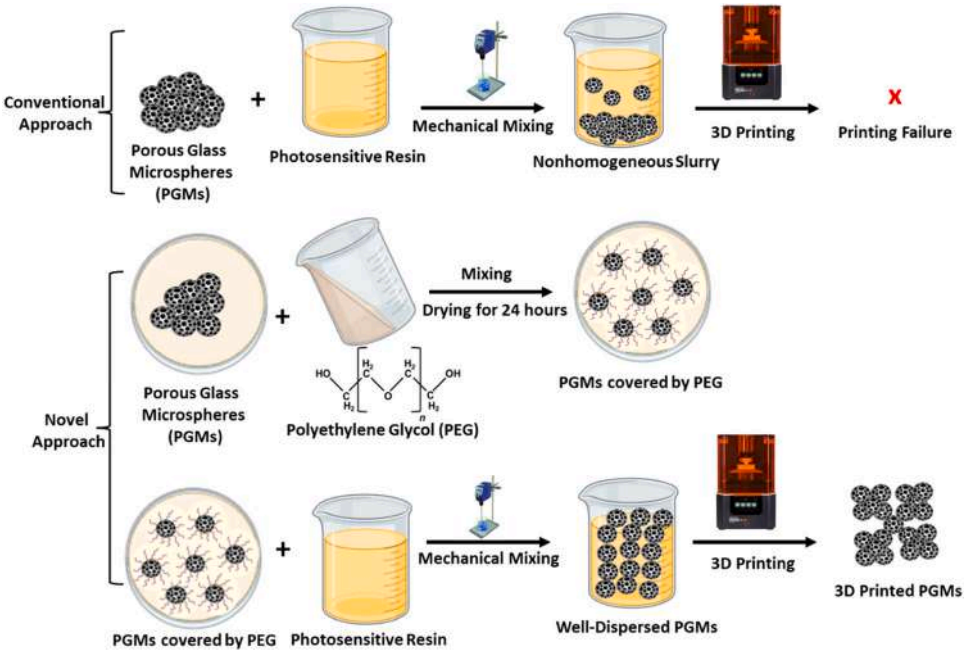

Fig. 1. Schematic diagram of 3d printing of PGMs scaffold by MSLA technique.

presented in Fig. 2a.

Slurries prepared from coated PGMs exhibited lower viscosities than other slurry formulations, including Resin+PGMs, and Resin-+PGMs+PEG, as shown in Fig. 2a. The novel approach helped optimize the dispersion and interaction of the components, resulting in a slurry with reduced viscosity. Other formulations showed irregular viscosity, indicating the instability of the slurry from shear rates of 50–400 s^{-1} , as presented in Fig. 2a. Under shear rates ranging from 1 to 50 s^{-1} (Fig. 2b), the slurry prepared using the novel approach exhibits rheological behavior similar to that of the pure photocurable resin, indicating improved printability compared to other formulations. Fig. 2c shows that no significant viscosity changes occur in the proposed new approach slurry and the pure resin at a constant shear rate after 90 min of setting time. This indicates that the proposed slurry exhibits purely shear-thinning (time-independent) behavior, meaning its viscosity stabilizes and remains slightly constant for 90 min. In contrast, the viscosity of the other formulations (PGMs + PEG + Resin and PGMs + Resin) increases progressively over time. This increase is primarily due to the segregation and sedimentation of porous glass microspheres within these formulations. As the microspheres gradually settle, their uniform distribution within the resin matrix decreases, leading to a time-dependent rise in viscosity. However, during the first 30 min, the viscosity of these formulations remained relatively stable (Fig. 2d). This behavior indicates instability in the suspension, which could negatively impact the consistency and reliability of the slurry during extended printing processes, as noted in the study [27].

Utilizing PEG-coated PGMs significantly improves the consistency of mixtures, thus avoiding separation. In this context, stability refers to the capacity of suspensions to uphold or rapidly restore a uniform particle distribution, which is essential for guaranteeing the excellence of the

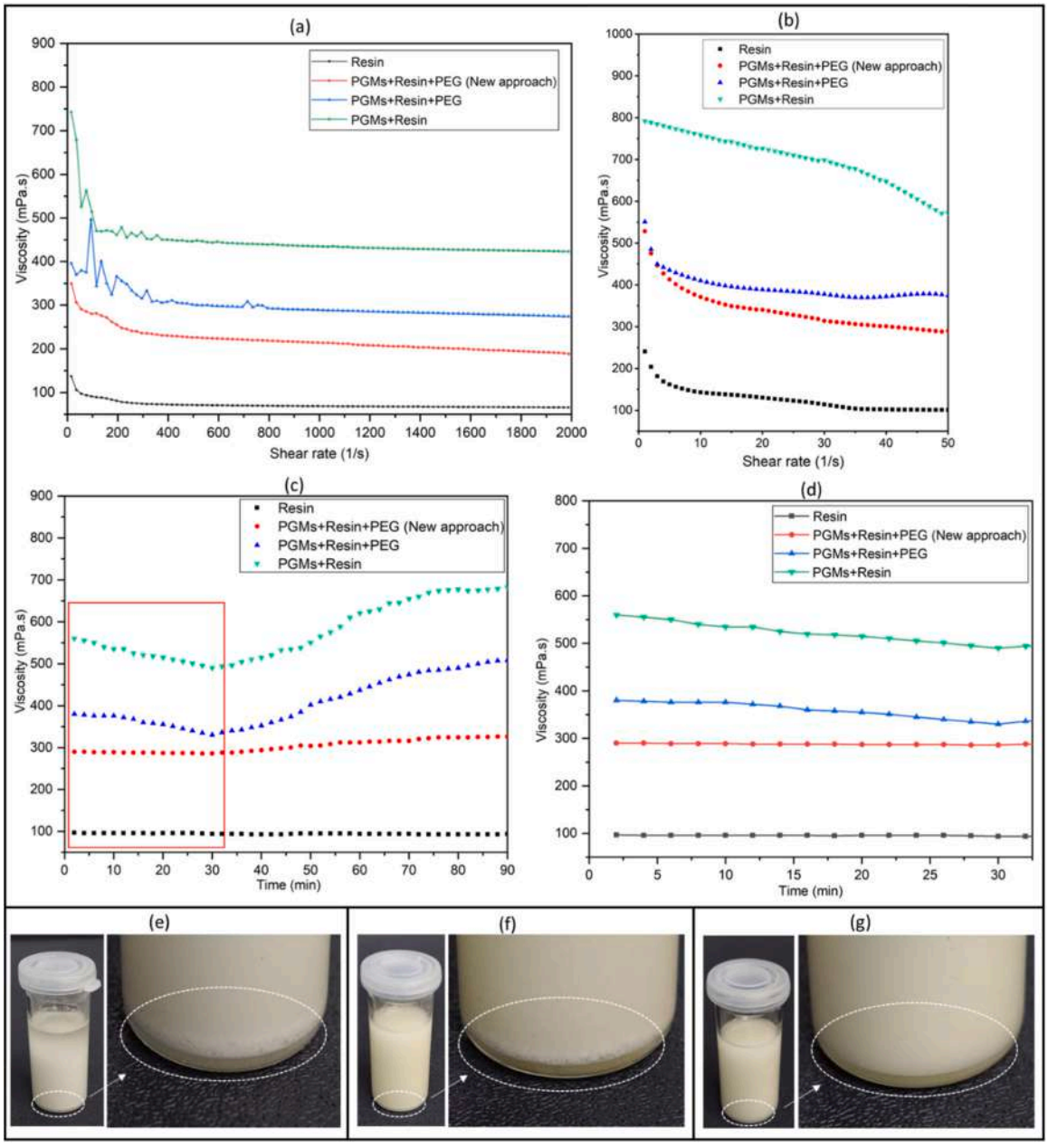

Fig. 2. (a) Viscosity of PGM suspensions prepared by different approaches as a function of shear rate (1–2000 s^{-1}), (b) Viscosity of PGM suspensions as a function of shear rate (1–50 s^{-1}), (c) Viscosity of PGM suspensions as a function of time at a shear rate of 50 s^{-1} , (d) Enlarged view of (c), showing the viscosity behavior over 30 min. Visual settling tests showing (e) high separation of the PGMs from the resin after 30 min (f) relatively low separation of the PGMs from the mixed resin with PEG after 30 min, (g) no separation of the PGMs from the slurry prepared by the novel approach.

printed result [27]. Heterogeneity in suspensions containing porous particles may arise from two primary factors: settling and binder leaching, as seen in Fig. 2e and f. Settling occurs when particles settle down because of gravity, whereas binder leaching is the separation of the binder from the solid phase caused by inadequate capillary forces. These processes often happen concurrently and may be differentiated by the degree of mobility shown by the particles or the fluid. The impeded settling in slurries of porous materials is primarily affected by particle-particle interactions, which result in distorted velocity fields and thus contribute to extended settling periods [28].

The new method reported in this work tackles these difficulties by using PEG-coated PGM particles. The application of the PEG coating improves the interactions between particles, resulting in a decrease in settling velocity and effectively prevents the development of sediment or creaming [28]. PEG may impart slight repulsion between the coated microspheres, further aiding in maintaining a dispersed state. This repulsion counteracts the natural tendency of microspheres to clump together in the resin matrix, promoting uniformity. Although PEG is hydrophilic and might initially seem incompatible with a hydrophobic acrylate resin, its function as a steric stabilizer, combined with potential polar interactions with resin components, can enhance dispersion. The PEG coating reduces the surface energy differences between the microspheres and the resin, which minimizes aggregation and facilitates a uniform distribution [27]. In addition, the PEG coating enhances the formation of more robust binder-particle connections by boosting the capacity of the binder to spread and adhere to the particles, hence reducing the amount of binder that is washed away [28]. The capillary forces between the binder and particles are effectively sustained, preventing the binder's detachment from the solid phase. Essentially, using PEG-coated PGM particles guarantees that the solution maintains a uniform distribution of particles throughout the procedure and printing, as seen in Fig. 2g. This is accomplished by reducing the speed at which particles in the slurry settle and by improving the binder's capacity to remain in place, limiting both settling and the leaching of the binder [27]. Consequently, this approach guarantees a consistent mixture of particles in the liquid, crucial for achieving excellent printing results.

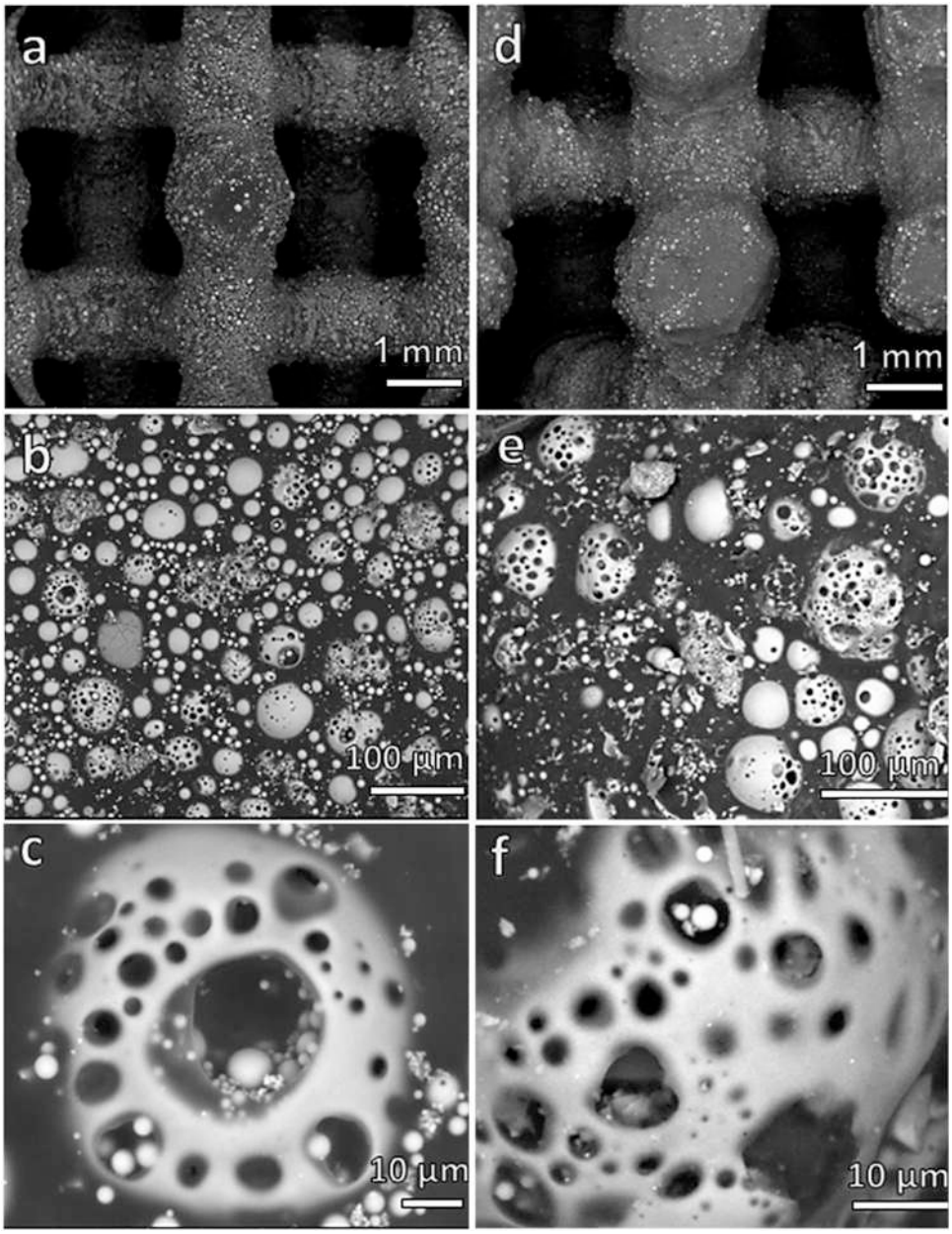

Fig. 3. SEM images of the green scaffolds (a, b, and c) prepared from PGMs and (d, e, and f) prepared from the combination of PGMs and TiO_2.

Fig. 3a and d demonstrate that the green scaffolds prepared from PGMs and PGMs with TiO_2 were defect-free for all formulations, resulting in components with particularly high resolution. The spherical PGM-particles were homogeneously distributed throughout the diamond cell structure (Figs. 3b and 2e). Fig. 3c and f show coated PGMs embedded in the photosensitive resin.

The printed component undergoes an incomplete curing process during printing and therefore requires subsequent curing. Post-curing is achieved using ultraviolet (UV) light, which can induce dimensional inaccuracies, potentially resulting in clearance and fitting issues. Primarily, the most prevalent problem involves variations in linear dimensions. The reference diamond cell structure (Fig. 4a, b) provides a baseline for comparing the fabricated scaffolds. The side and top views reveal a uniform, repeating pattern consisting of 1.5 mm balls connected with 0.95 mm thick sticks, which can be used to analyze dimensional changes during post-fabrication. Specifically, the stick and ball thickness of the green printed parts increased by 17 % and 21 % (Fig. 4c) and 33 % and 42 % (Fig. 4d), respectively, for scaffolds fabricated from PGMs and PGMs with TiO_2, compared to the adopted model structure used as a reference. The addition of TiO_2 to the resin matrix significantly increased the size of the printed structure since titania causes intense light bending and scattering of the UV light. This will likely result in more noticeable swelling and distortion during curing (Fig. 4d) [21].

The high cooling rate characteristic for the flame synthesis, compared to the conventional melt quenching method, prevented any crystallization of the obtained PGMs. Preserving the produced pores of PGMs during sintering is a prerequisite for creating the hierarchical porosity required for water treatment applications [22,29]. The sintering kinetics of glass are influenced by (i) the crystallization of glass and (ii) the densification of the green body by viscous flow [30]. The glass transition marks the transition from glass to a liquid state, enabling viscous flow densification. On the other hand, the crystallization temperature marks the appearance of rigid inclusions in the softened glass mass, increasing viscosity. Apart from homogeneous shrinkage, this phenomenon controls the "freezing" of the shape of the green object [31].

Applying sintering at 1000°C under air conditions resulted in partial densification of the structure, indicating substantial porosity retention. SEM images of printed PGMs after sintering are shown in Fig. 5. Sintering of pure PGMs was successful at 1000 °C without any deformation of the designed model (Fig. 5a). Debinding and firing resulted in permeable struts, as documented by the microstructures in Fig. 5b and c, which showed angular PGMs particles connected only by necks. Adding TiO_2 retarded the sintering of the glass particles, and TiO_2 partially blocked the necking of the glass particles, hindering the viscous flow of glass and resulting in a partially deformed structure (Fig. 5d). Several studies have reported that the addition of TiO_2 to glass matrices impairs the sintering process [32,33], as the presence of rigid ceramic inclusions delays viscous flow. During sintering, the glass matrix must undergo softening and flow to enable the rearranging of particles and achieve densification [32,33]. On the other hand, increased porosity is one of the main reasons for the reduced strength, as pores act as stress concentrators and can cause failure of the sintered body [34].

Due to the deficiency in sintering by TiO_2 inclusion (Fig. 5e and f), adding silicone polymer as a binder supplement improved the integrity of titania-containing scaffolds (Fig. 6a–d). Silicone polymer is an organosilicon compound that thermally decomposes in air between 500–600°C, producing a silica-rich ceramic residue rather than completely volatilizing like conventional organic binders, as described in the studies [35,36]. This residue physically reinforces the green body

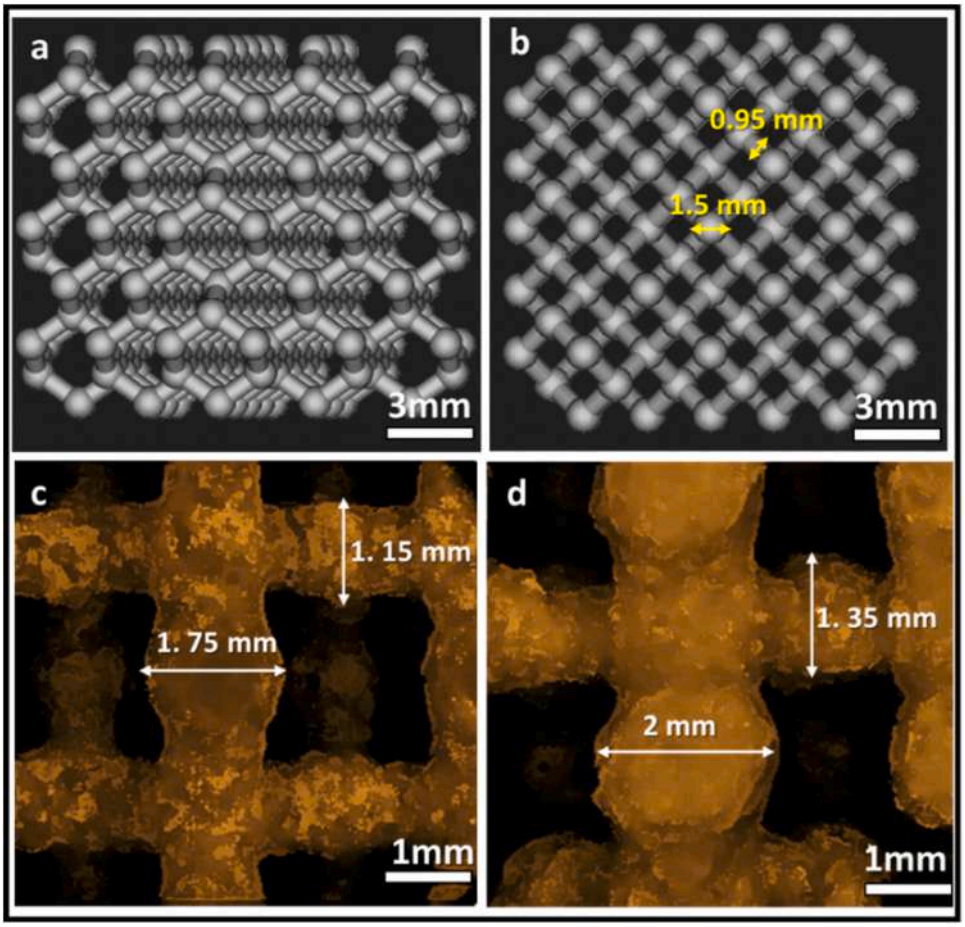

Fig. 4. Diamond cell structure adopted for MSLA (a) side view, (b) top view, top view of the green scaffolds, (c) made of PGMs, and (d) made of PGMs and TiO_2.

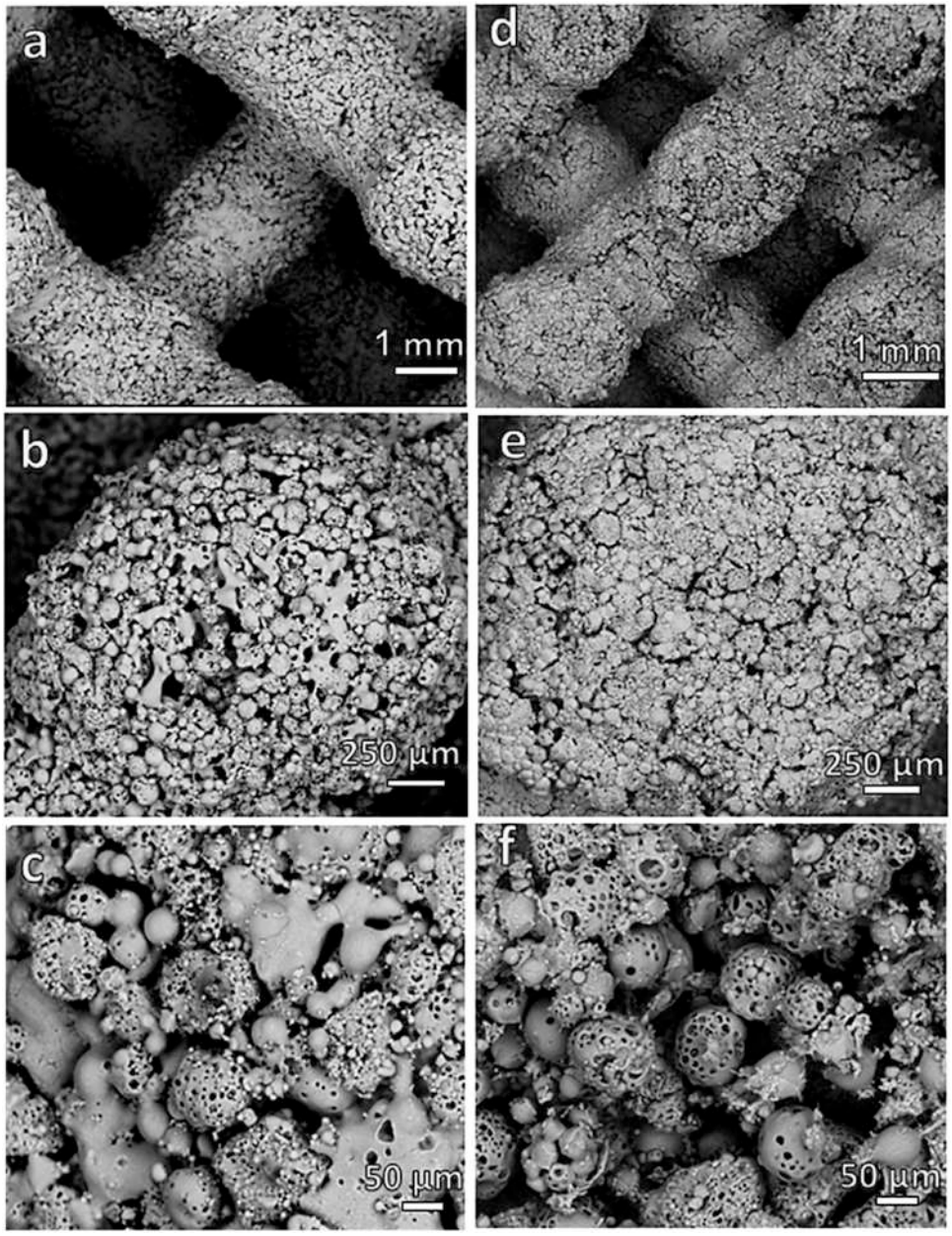

Fig. 5. SEM of the sintered scaffolds at 1000°C (a, b, and c) prepared from PGMs and (d, e, and f) prepared from PGMS and TiO_2.

by occupying interparticle voids, improving packing density, and forming physical bridges between microspheres, thereby enhancing pre-sintering strength and structural integrity before viscous flow begins [29]. The effect of the silicone polymer at this stage is primarily physical, providing early-stage stabilization and maintaining the dimensional stability of the scaffold. However, at higher temperatures (1000°C), the silica residue may also engage in chemical interactions with the glass matrix, forming silicate networks that promote necking and enhance viscous flow, thus partially mitigating the sintering inhibition caused by TiO_2. The presence of silicone-derived silica may reduce this hindrance by forming calcium titanosilicate phase, evident in the XRD analysis (Fig. 7).

Covering the TiO_2 nanoparticles with the Silicone polymer helps connect the glass microspheres, decreasing porosity and increasing mechanical properties (see Table 1). As illustrated in Fig. 6C, spherical particles are embedded in the silicone matrix, providing sufficient binding and strength. Uniformity of the structure was achieved, as shown in Fig. 6a. Only necking of adjacent particles may be detected (Fig. 6d), maintaining the shapes of the spheres and overall geometry regular (Fig. 6a and b).

The high solid loading, by maximizing the packing density, prevents any significant slipping of particles after debinding and crystallization. The applied sintering temperature avoids the grain roughness and the viscous collapse of the struts [37]. The total porosity of the printed PGMs is 90 %, completely open, due to the uniform distribution of the particles of the geometric model used for printing and the pores within the microspheres (Table 1). The form of the spheres remains unchanged throughout sintering. Alternatively, glass viscosity may be determined as an Arrhenius function of temperature [29].

Sintering of the printed scaffold (PGMs) at 1000°C resulted in the formation of wollastonite ($CaSiO_3$) (PDF 85–0654) due to the higher ratios of calcia and silica in the glass composition. The scaffold prepared from PGMs with silicone polymer and TiO_2 (PGMs+TiO_2+Si) resulted in the formation of Ti-containing phases such as calcium titanosilicate ($Ca_4Ti_4Si_4O_{20}$) (COD 96–900–2440), and rutile (TiO_2) (COD 96–900–4144) in addition to the wollastonite phase, as presented in

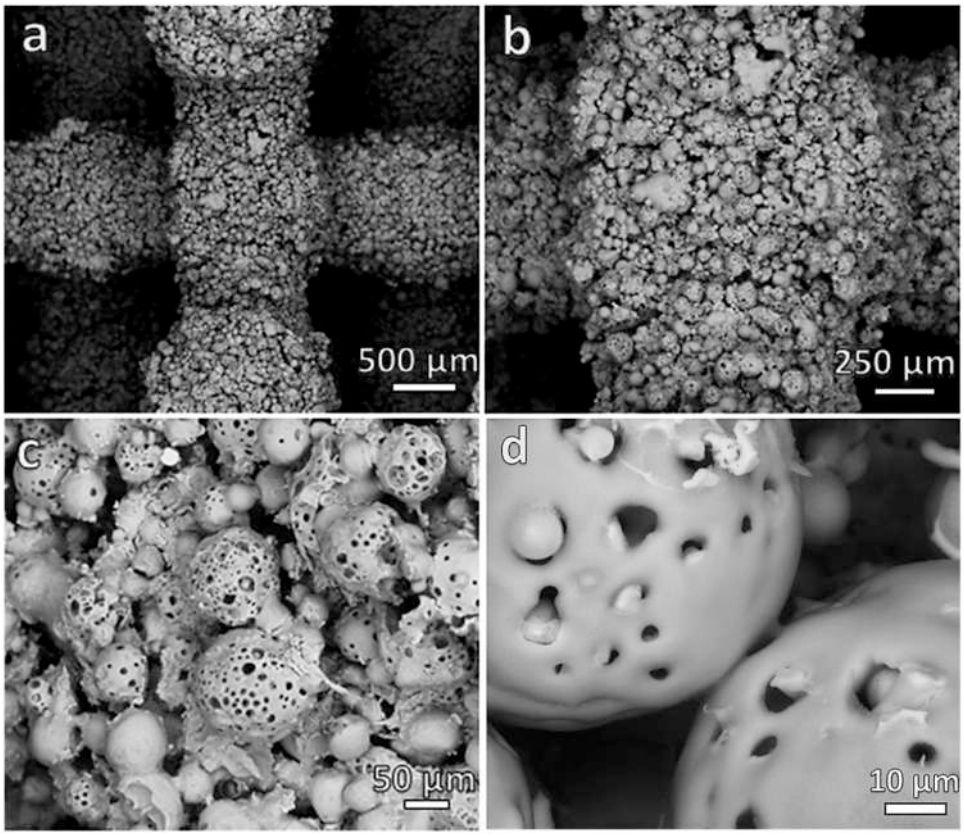

Fig. 6. SEM images of the sintered scaffolds at 1000°C (a, b, c and d) PGMs with TiO_2 and the silicone polymer.

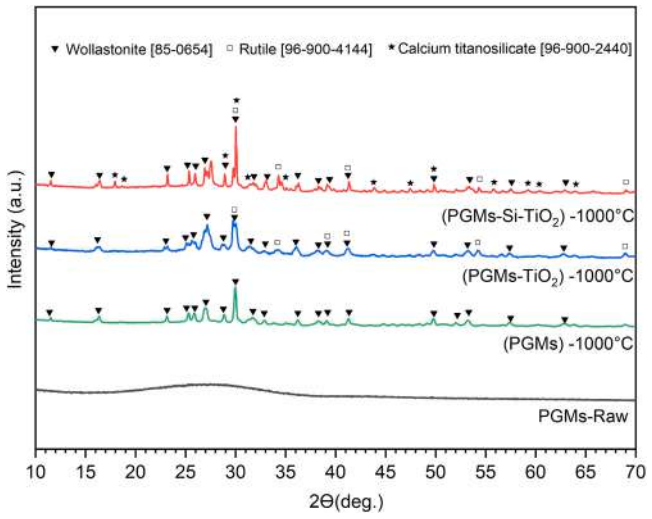

Fig. 7. XRD patterns of basic PGMs and 3D printed scaffolds from PGMs after sintering at 1000°C.

Fig. 7.

The results of the measurements of compressive strength and porosity are summarized in Table 2. The printed samples with the largest porosity exhibited poor mechanical strength. However, using the silicone binder resulted in a significant (100 %) enhancement in compressive strength, demonstrating the crucial role of the binder in improving the mechanical properties of printed samples. According to the studies reported by Gibson and Ashby [38], a highly porous ceramic lattice or sponge has a compressive strength determined by the formula:

$$\sigma_c \approx 0.2 \times \sigma_{bend} \times \rho_{rel}^{1.5}$$

where ρ_{rel} is the relative density ($\rho_{rel} = 1 - P/100$), P is the total porosity, and σ_{bend} is the bending strength of the solid phase positioned in the struts. By inverting the equation, values of σ_{bend*} can be obtained from the experimentally determined compressive strength and porosity (see Table 2). The significant difference (from 32 to 63 MPa) confirms the progress achieved by adding a silicone binder [38].

The Atomic Force Microscopy (AFM) images of 3D printed PGMs+TiO_2+Si obtained before and after sintering give insights into the structural and surface changes caused by the sintering process. Before sintering, the AFM picture had a very smooth topology with high printing quality (Fig. 8a), as demonstrated by an average roughness value of about 70 nm (Fig. 8b). This smoothness is due to the careful deposition of photosensitive resin during the 3D printing. After sintering

Table 2
Physical and mechanical properties of the printed scaffolds.

Samples	Geometrical density (g/cm^3)	Apparent density (g/cm^3)	True density (g/cm^3)	Open porosity (%)	Compressive strength (MPa)	Bending Strength (MPa)
PGMs	0.21 ± 0.01	2.66 ± 0.03	2.80 ± 0.03	91 ± 1	0.2 ± 0.1	37
PGMs+TiO_2	0.24 ± 0.01	2.75 ± 0.03	2.90 ± 0.02	90 ± 1	0.2 ± 0.1	32
PGMs+TiO_2+Si	0.21 ± 0.03	2.62 ± 0.02	2.85 ± 0.02	90 ± 2	0.4 ± 0.1	63

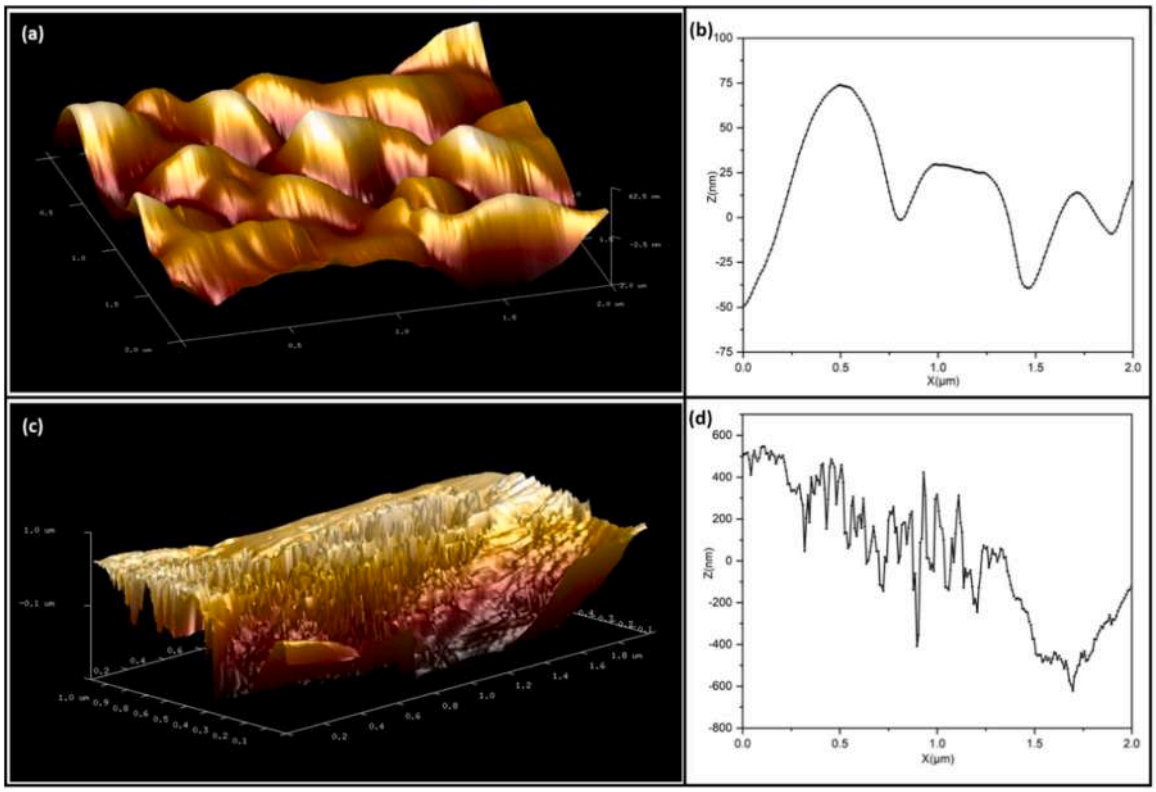

Fig. 8. Atomic force microscopy enabled surface roughness measurement of (a) green 3D printed PGMs+TiO_2+Si, (b) surface roughness before sintering, (c) sintered 3D printed PGMs+TiO_2+Si (d) surface roughness after sintering.

and removing the photosensitive resin, the AFM picture showed a considerable change in surface morphology. The formerly smooth surface had become noticeably rougher and sharper (Fig. 8c), with an average roughness value of about 500 nm (Fig. 8d).

The debinding and sintering procedure had a profound effect on the glass structure, as seen by the surface morphology (Fig. 5). Surface roughness increases in large part due to the occurrence of viscous flow during sintering. The glass undergoes a phase transition from solid to liquid as it heats and fuses. Particle rearrangement and surface flaws are the outcomes of flow within sintered glass caused by this phase transition. After sintering, the surface imperfections shown in the AFM picture cause the roughness values to be larger (Fig. 8c and d).

Beyond structural modifications, the roughened surface produced by debinding and sintering may have significant practical effects. Increasing the surface roughness may improve the availability of active sites for adsorption processes. In particular, the higher surface area and greater surface roughness can provide additional binding sites for molecules like methylene blue, potentially improving the capacity for material adsorption.

3.1. Methylene blue remediation

Fig. 9a presents the absorbance spectrum of a methylene blue solution (50 mg/L) in deionized water. The maximum absorbance at 664 nm serves as the reference for the initial dye concentration (C_0). The adsorption of methylene blue is discerned by the reduction in absorbance resulting from immersing the samples in a methylene blue solution in the absence of light. In Fig. 9b, it is illustrated that the maximum adsorption efficiency, attained within 120 min, reached 70 and 74 % for the samples labelled as PGMs and PGMs+TiO_2. The sensitivity to UV degradation of the specific organic species is inferred from the decline in absorbance after 60 min of irradiation. Furthermore, Fig. 9c illustrates that the decrease in methylene blue content is intensified in samples PGMs+TiO_2 and PGMs+TiO_2+Si, with removal efficiencies of 73 % and 77 %, respectively, where $C/C_0 = 0.27$ and 0.23, respectively. Exposure intervals of up to 75 min resulted in negligible absorbance, suggesting that the methylene blue dye was completely removed from the solution for both PGMs+TiO_2 and PGMs+TiO_2+Si, as shown in Fig. 9d.

The transport of methylene blue through the 3D porous glass microspheres scaffold is facilitated by the presence of multiple entry and exit pathways within each microsphere. Additionally, the partially charged surface of the glass microspheres enables electrostatic interactions with the cationic methylene blue molecules, further complemented by hydrogen bond formation [22]. These interactions collectively enhance the adsorption efficiency of the dye. On the other hand, scaffolds containing TiO_2, upon exposure to UV light, absorb photons with energy equal to or greater than their bandgap energy, leading to the generation of electron-hole pairs. The excited electrons (e^-) transition to the conduction band, while the holes (h^+) remain in the valence band. These charge carriers initiate redox reactions, where the holes oxidize water molecules to produce hydroxyl radicals (OH•), and the electrons reduce oxygen molecules to form superoxide radicals ($O_2•^-$). Reactive oxygen species (ROS) act as powerful oxidizing agents that target methylene blue dye molecules, breaking down their complex structure into smaller, non-toxic byproducts such as CO_2, H_2O, and inorganic ions [39].

Catalyst deactivation and regeneration are important aspects to consider when expanding heterogeneous photocatalysis due to economic implications [39]. The strong adsorption and interaction between the active sites on the catalyst surface and the oxygen-containing intermediate reactions lead to a sudden decrease in the active sites during the reaction of the reactant [40]. Several types of reactivation approaches have been examined to regenerate deactivated photocatalysts, including the use of chemicals (HNO_3, NaOH, NH_4OH, H_2O_2 with or without UV irradiation), washing with water [39,41–45], ultrasonic treatment with water and methanol [46], and thermal processes [47].

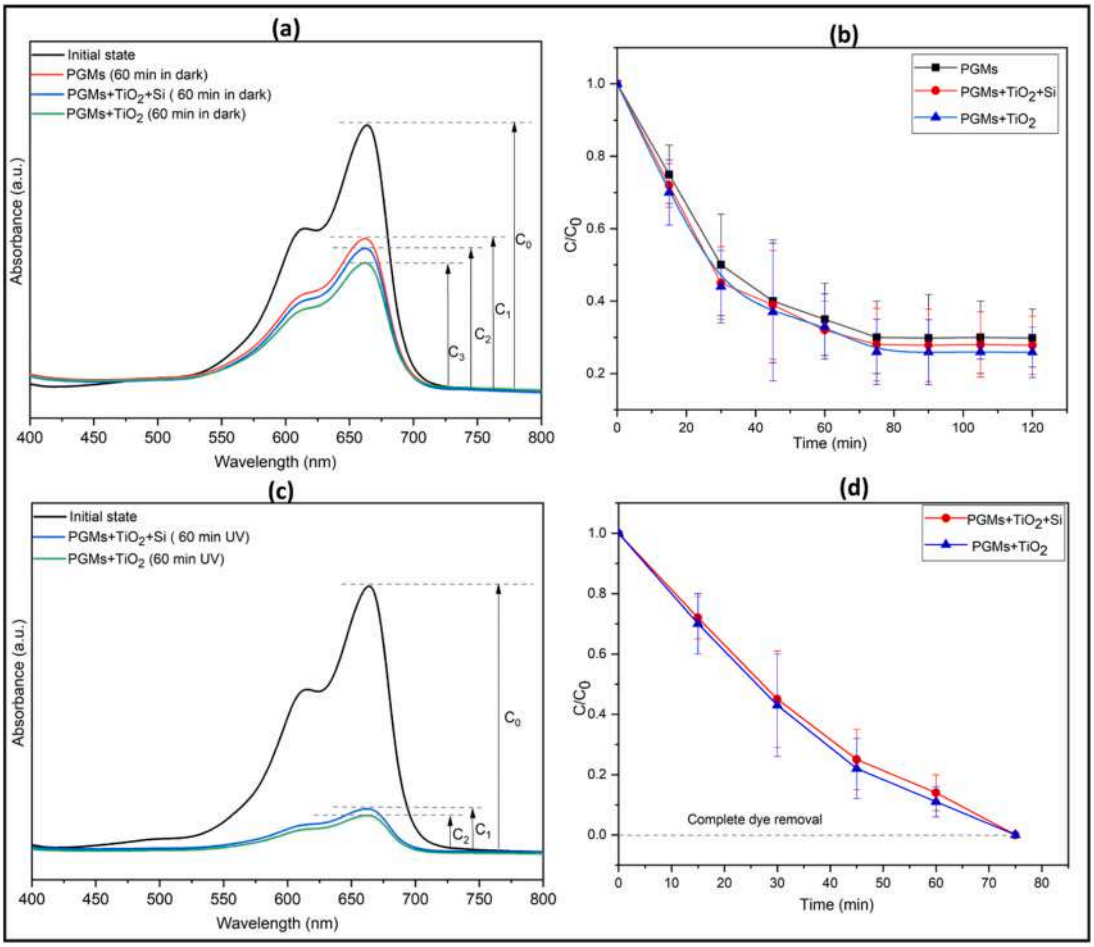

Fig. 9. (a) Absorption spectra of the methylene blue solution in the initial state and after 60 min in contact with 3D printed scaffolds in dark, (b) evolution of the relative concentration of methylene blue with increasing the adsorption time, (c) Absorption spectra of the methylene blue solution in the initial state and after 60 min in contact with 3D printed scaffolds under UV exposure, (d) evolution of the relative concentration of methylene blue with increasing UV exposition time.

However, the previous treatments are costly and have a negative impact on the environment. In the current study, reactivation was much more accessible by only exposing the samples to UV light. To verify the recyclability of the printed scaffolds, they were subjected to 5 consecutive degradation cycles to evaluate the preservation of their photodegradation ability. After each cycle, the scaffolds were exposed to a UV lamp for 1 h. The 3D printed scaffold after 5 cycles is shown in Fig. 10a. The degradation performance of methylene blue after 5 cycles was nearly 90 %, as shown in Fig. 10b. EDS of the scaffold's cross section after regeneration revealed the characteristic elements of the previously documented phases, including rutile and wollastonite (Fig. 10c).

The 3D-printed scaffolds composed of porous glass microspheres with titania (PGMs+TiO_2+Si) exhibit superior degradation efficiency compared to TiO_2–ceramic [48], TiO_2 [49], TiO_2–glass spheres [50], and TiO_2–hollow fiber structures [51]. Furthermore, their degradation performance is comparable to that of silver TiO_2 films [52] and TiO_2 polymeric substrates [53]. However, in the present study, the complete degradation of methylene blue was achieved in a significantly shorter time (75 min) than in previously reported studies (110–240 min) [48–53]. This enhanced efficiency can be attributed to the scaffold's substantial open porosity (90 %), which provides an extensive surface area, facilitating greater interaction between the photocatalyst and methylene blue dye molecules. The high porosity promotes efficient dye adsorption onto the scaffold, thereby improving degradation efficiency. Additionally, the synergistic combination of TiO_2 nanoparticles and porous glass microspheres enhances photocatalytic activity by preventing nanoparticle agglomeration and maintaining a high surface area for reaction. The interconnected porous network also optimizes light penetration throughout the scaffold, ensuring uniform activation of TiO_2 nanoparticles under light exposure. This optimized activation process significantly accelerates the degradation rate, contributing to the scaffold's superior photocatalytic performance.

4. Conclusion

This study showcases the sustainable potential of 3D printing in glass upcycling by transforming fiberglass waste into functional materials through a structured process involving alkali activation, flame synthesis, and MSLA printing. Coating porous glass microspheres with PEG improved their dispersion in resin, enabling the successful fabrication of highly porous (90 %) diamond-shaped scaffolds. Incorporating 7.5 wt% TiO_2 endowed the scaffolds with photocatalytic properties but introduced sintering challenges, which were effectively mitigated by adding a silicone polymer binder. Post-sintering analysis revealed increased surface roughness, enhancing adsorption capacity. The 3D-printed scaffolds achieved complete photodegradation of methylene blue within 75 min and retained over 90 % efficiency over multiple cycles, performing competitively with existing titania-based photocatalysts. Overall, this work highlights a cost-effective, eco-friendly approach to converting glass waste into advanced materials for environmental remediation.

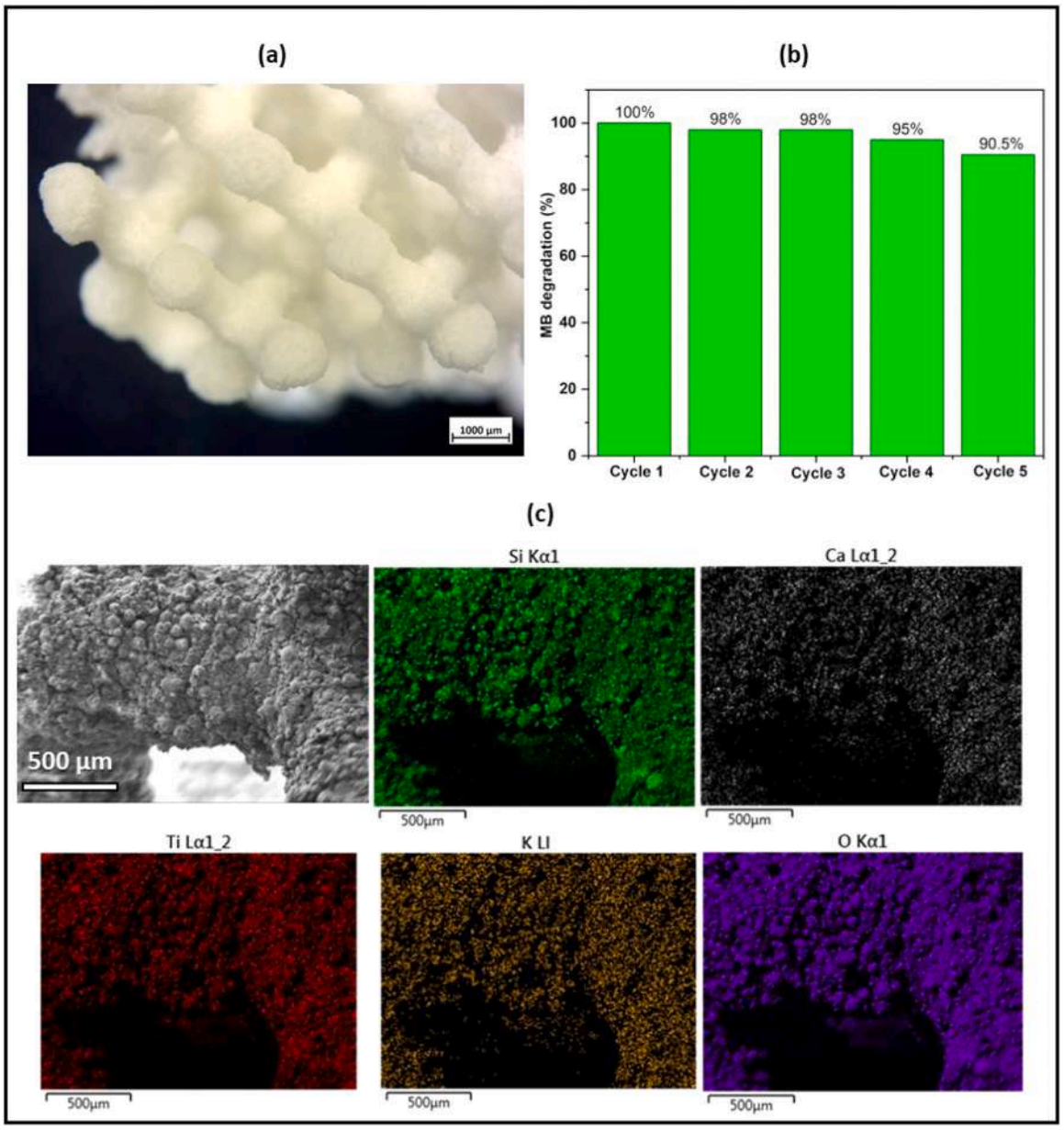

Fig. 10. (a) The 3D scaffold after five consecutive cycles, (b) Evolution of methylene blue degradation (%) with the number of cycles, (c) EDS of the cross-section of the recycled scaffolds after five consecutive cycles.

CRediT authorship contribution statement

Mokhtar Mahmoud: Writing – review & editing, Writing – original draft, Visualization, Methodology, Investigation, Formal analysis. **Hamada Elsayed:** Writing – review & editing, Supervision, Project administration, Methodology, Investigation, Conceptualization. **Jozef Kraxner:** Writing – review & editing, Visualization, Supervision. **Martin Michálek:** Writing – review & editing, Methodology, Investigation. **Beáta Pecušová:** Writing – review & editing, Methodology, Investigation. **Montaha Anjass:** Writing – review & editing, Methodology, Investigation. **Nikhil Arya:** Writing – review & editing, Methodology, Investigation. **Enrico Bernardo:** Writing – review & editing, Supervision, Funding acquisition, Conceptualization. **Dušan Galusek:** Writing – review & editing, Validation, Funding acquisition.

Declaration of Competing Interest

The authors declare that they have no known competing financial interests or personal relationships that could have appeared to influence the work reported in this paper.

Acknowledgements

This paper is a part of the dissemination activities of the project FunGlass. This project has received funding from the European Unionś Horizon 2020 research and innovation program under grant agreement No 739566. Publication was created also in the frame of project: Advancement and support of R&D for Centre for diagnostics and quality testing of materials in the domains of the RIS3 SK specialization, ITMS2014 + :313011W442, based on the Operational Programme Integrated Infrastructure and funded from the European Regional Development Fund. The authors also gratefully acknowledge the financial support from the project APVV-23-0352 and the CLiCAM Project (HORIZON-WIDERA-2022-TALENTS-03, Grant No. 101120555).

Appendix A. Supporting information

Supplementary data associated with this article can be found in the online version at doi:10.1016/j.jeurceramsoc.2025.117651.

References

[1] O.J. Fisher, N.J. Watson, J.E. Escrig, R.L. Gomes, Intelligent resource use to deliver waste valorisation and process resilience in manufacturing environments, Johns. Matthey Technol. Rev. 64 (2020) 93–99, https://doi.org/10.1595/205651320X15735483214878.

[2] M. Lieder, A. Rashid, Towards circular economy implementation: a comprehensive review in context of manufacturing industry, J. Clean. Prod. 115 (2016) 36–51, https://doi.org/10.1016/j.jclepro.2015.12.042.

[3] E. Bernardo, G. Scarinci, P. Colombo, Vitrification of waste and reuse of waste-derived glass. Encyclopedia of Sustainability Science and Technology, Springer New York, New York, NY, 2012, pp. 11581–11613, https://doi.org/10.1007/978-1-4419-0851-3_96.

[4] M. Hujova, P. Rabelo Monich, H. Kankova, H. Lucas, B. Xakalashe, B. Friedrich, J. Kraxner, D. Galusek, E. Bernardo, New glass-based binders from engineered mixtures of inorganic waste, Int. J. Appl. Glass Sci. 12 (2021) 570–580, https://doi.org/10.1111/ijag.16262.

[5] S.A. Samad, A. Arafat, E. Lester, I. Ahmed, Upcycling glass waste into porous microspheres for wastewater treatment applications: efficacy of dye removal, Mater 15 (2022), https://doi.org/10.3390/ma15175809.

[6] A. Cescon, J.-Q. Jiang, Filtration process and alternative filter media material in water treatment, Water 12 (2020) 3377, https://doi.org/10.3390/w12123377.

[7] J. Bové, G. Arbat, M. Duran-Ros, T. Pujol, J. Velayos, F. Ramírez de Cartagena, J. Puig-Bargués, Pressure drop across sand and recycled glass media used in micro irrigation filters, Biosyst. Eng. 137 (2015) 55–63, https://doi.org/10.1016/j.biosystemseng.2015.07.009.

[8] G. Wang, L. Xu, J. Zhang, T. Yin, D. Han, Enhanced photocatalytic activity of powders (P25) via calcination treatment, Int. J. Photoenergy 2012 (2012) 1–9, https://doi.org/10.1155/2012/265760.

[9] Y. Kim, H.M. Hwang, L. Wang, I. Kim, Y. Yoon, H. Lee, Solar-light photocatalytic disinfection using crystalline/amorphous low energy bandgap reduced TiO2, Sci. Rep. 6 (2016) 25212, https://doi.org/10.1038/srep25212.

[10] J. Wang, M. Wang, Y. Tian, W. Deng, A review on photocatalytic glass ceramics: fundamentals, preparation, performance enhancement and future development, Catalysts 12 (2022) 1235, https://doi.org/10.3390/catal12101235.

[11] D. Chahar, D. Kumar, P. Thakur, A. Thakur, Visible light induced photocatalytic degradation of methylene blue dye by using Mg doped Co-Zn nanoferrites, Mater. Res. Bull. 162 (2023) 112205, https://doi.org/10.1016/j.materresbull.2023.112205.

[12] S. Sawalha, R. Hamed, M. Assali, Parameters affecting methylene blue dye photodegradation by carbon dots prepared from olive pomace, ChemistrySelect 8 (2023), https://doi.org/10.1002/slct.202300522.

[13] M. Mahmoud, J. Kraxner, H. Elsayed, E. Bernardo, D. Galusek, Fabrication and environmental applications of glass microspheres: a review, Ceram. Int. 49 (2023) 39745–39759, https://doi.org/10.1016/j.ceramint.2023.10.040.

[14] M. Mahmoud, J. Kraxner, H. Elsayed, F.M. Stabile, M. Michálková, D. Galusek, E. Bernardo, Enhanced methylene blue adsorption by double alkali activation of highly porous glass microspheres prepared from waste glass, J. Mater. Sci. 59 (2024) 73–85, https://doi.org/10.1007/s10853-023-09207-7.

[15] X. Jaramillo-Fierro, S. Gaona, J. Ramón, E. Valarezo, Porous geopolymer/ZnTiO3/TiO2 composite for adsorption and photocatalytic degradation of methylene blue dye, Polymers 15 (2023) 2697, https://doi.org/10.3390/polym15122697.

[16] A. Kulis-Kapuscinska, M. Kwoka, M.A. Borysiewicz, T. Wojciechowski, N. Licciardello, M. Sgarzi, G. Cuniberti, Photocatalytic degradation of methylene blue at nanostructured ZnO thin films, Nanotechnology 34 (2023) 155702, https://doi.org/10.1088/1361-6528/aca910.

[17] J.M. Aguirre-Cortés, A.I. Moral-Rodríguez, E. Bailón-García, A. Davó-Quiñonero, A. F. Pérez-Cadenas, F. Carrasco-Marín, 3D printing in photocatalysis: methods and capabilities for the improved performance, Appl. Mater. Today 32 (2023) 101831, https://doi.org/10.1016/j.apmt.2023.101831.

[18] P. Ożóg, H. Elsayed, L. Grigolato, G. Savio, J. Kraxner, D. Galusek, E. Bernardo, Engineering of silicone-based blends for the masked stereolithography of biosilicate/carbon composite scaffolds, J. Eur. Ceram. Soc. 42 (2022) 6192–6198, https://doi.org/10.1016/j.jeurceramsoc.2022.06.057.

[19] J. Yu, X. Zhao, Effect of surface treatment on the photocatalytic activity and hydrophilic property of the sol-gel derived TiO2 thin films, Mater. Res. Bull. 36 (2001) 97–107, https://doi.org/10.1016/S0025-5408(00)00475-X.

[20] T. Nishida, A. Morimoto, Y. Yamamoto, S. Kubuki, Waste water purification using new porous ceramics prepared by recycling waste glass and bamboo charcoal, Appl. Water Sci. 7 (2017) 4281–4286, https://doi.org/10.1007/s13201-017-0561-1.

[21] Y. Zhu, T. Tang, S. Zhao, D. Joralmon, Z. Poit, B. Ahire, S. Keshav, A.R. Raje, J. Blair, Z. Zhang, X. Li, Recent advancements and applications in 3D printing of functional optics, Addit. Manuf. 52 (2022) 102682, https://doi.org/10.1016/j.addma.2022.102682.

[22] M. Mahmoud, J. Kraxner, H. Elsayed, D. Galusek, E. Bernardo, Advanced dye sorbents from combined stereolithography 3D printing and alkali activation of pharmaceutical glass waste, Materials 15 (2022) 6823, https://doi.org/10.3390/ma15196823.

[23] M. Mahmoud, J. Kraxner, H. Kaňková, M. Hujová, S. Chen, D. Galusek, E. Bernardo, Porous glass microspheres from alkali-activated fiber glass waste, Materials 15 (2022) 1043, https://doi.org/10.3390/ma15031043.

[24] K. Zhang, C. Xie, G. Wang, R. He, G. Ding, M. Wang, D. Dai, D. Fang, High solid loading, low viscosity photosensitive Al2O3 slurry for stereolithography based additive manufacturing, Ceram. Int. 45 (2019) 203–208, https://doi.org/10.1016/j.ceramint.2018.09.152.

[25] M.G.J.W. Halloran T.-M. Chu, Stereolithography Resin for Rapid Prototyping of Ceramics and Metals, US Patent 6,117,612 (2000).

[26] Y. Gao, J. Lalevée, A. Simon-Masseron, An overview on 3D printing of structured porous materials and their applications, Adv. Mater. Technol. 8 (2023), https://doi.org/10.1002/admt.202300377.

[27] P. Cai, L. Guo, H. Wang, J. Li, J. Li, Y. Qiu, Q. Zhang, Q. Lue, Effects of slurry mixing methods and solid loading on 3D printed silica glass parts based on DLP stereolithography, Ceram. Int. 46 (2020) 16833–16841, https://doi.org/10.1016/j.ceramint.2020.03.260.

[28] G. Fei, C. Parra-Cabrera, Y. Li, D.E. Kravchenko, R. Dochy, L. Van Looy, R. Ameloot, Stereolithographic 3D printing of graded porous materials via an integrated digital exposure and selective dissolution strategy, Cell Rep. Phys. Sci. 4 (2023) 101504, https://doi.org/10.1016/j.xcrp.2023.101504.

[29] J. Kraxner, H. Elsayed, A. Dasan, M. Hujová, M. Michálková, M. Michálek, E. Bernardo, D. Galusek, Additive manufacturing of Ca–Mg silicate scaffolds supported by flame-synthesized glass microspheres, Ceram. Int. (2021), https://doi.org/10.1016/j.ceramint.2021.12.095.

[30] M. Michálková, J. Kraxner, M. Michálek, D. Galusek, Preparation of translucent YAG glass/ceramic at temperatures below 900 °C, J. Eur. Ceram. Soc. 40 (2020) 2581–2585, https://doi.org/10.1016/j.jeurceramsoc.2019.11.011.

[31] G.W. Scherera, Sintering with rigid inclusions, J. Am. Ceram. Soc. 70 (1987) 719–725, https://doi.org/10.1111/j.1151-2916.1987.tb04870.x.

[32] L.A. Bicalho, C.A.R.P. Baptista, R.C. Souza, C. Santos, K. Strecker, M.J.R. Barboza, Fatigue and subcritical crack growth in ZrO2–bioglass ceramics, Ceram. Int. 39 (2013) 2405–2414, https://doi.org/10.1016/j.ceramint.2012.08.093.

[33] R.B.P. Miranda, W.G.J. Miranda, D.R.R. Lazar, V. Ussui, J. Marchi, P.F. Cesar, Effect of titania content and biomimetic coating on the mechanical properties of the Y-TZP/TiO2 composite, Dent. Mater. 34 (2018) 238–245, https://doi.org/10.1016/j.dental.2017.11.003.

[34] H.N. Yoshimura, A.L. Molisani, N.E. Narita, P.F. Cesar, H. Goldenstein, Porosity dependence of elastic constants in aluminum nitride ceramics, Mater. Res. 10 (2007) 127–133, https://doi.org/10.1590/s1516-14392007000200006.

[35] H. Elsayed, M. Picicco, A. Dasan, J. Kraxner, D. Galusek, E. Bernardo, Glass powders and reactive silicone binder: interactions and application to additive manufacturing of bioactive glass-ceramic scaffolds, Ceram. Int. 45 (2019) 13740–13746, https://doi.org/10.1016/j.ceramint.2019.04.070.

[36] H. Elsayed, M. Picicco, A. Dasan, J. Kraxner, D. Galusek, E. Bernardo, Glass powders and reactive silicone binder: application to digital light processing of bioactive glass-ceramic scaffolds, Ceram. Int. 46 (2020) 25299–25305, https://doi.org/10.1016/j.ceramint.2020.06.323.

[37] A. Dasan, A. Talimian, J. Kraxner, D. Galusek, H. Elsayed, E. Bernardo, Åkermanite glass microspheres: preparation and perspectives of sinter-crystallization, Int. J. Appl. Glass Sci. 12 (2021) 551–561, https://doi.org/10.1111/ijag.16115.

[38] A. Dasan, J. Kraxner, L. Grigolato, G. Savio, H. Elsayed, D. Galusek, E. Bernardo, 3D printing of hierarchically porous lattice structures based on akermanite glass microspheres and reactive silicone binder, J. Funct. Biomater. 13 (2022), https://doi.org/10.3390/jfb13010008.

[39] N. Miranda-García, S. Suárez, B. Sánchez, J.M. Coronado, S. Malato, M. I. Maldonado, Photocatalytic degradation of emerging contaminants in municipal wastewater treatment plant effluents using immobilized TiO2 in a solar pilot plant, Appl. Catal. B 103 (2011) 294–301, https://doi.org/10.1016/j.apcatb.2011.01.030.

[40] O. Prieto, J. Fermoso, R. Irusta, Photocatalytic degradation of toluene in air using a fluidized bed photoreactor, Int. J. Photoenergy 2007 (2007) 1–8, https://doi.org/10.1155/2007/32859.

[41] R. Portela, B. Sánchez, J.M. Coronado, R. Candal, S. Suárez, Selection of TiO2-support: UV-transparent alternatives and long-term use limitations for H2S removal, Catal. Today 129 (2007) 223–230, https://doi.org/10.1016/j.cattod.2007.08.005.

[42] M. Kanna, S. Wongnawa, S. Buddee, K. Dilokkhunakul, P. Pinpithak, Amorphous titanium dioxide: a recyclable dye remover for water treatment, J. Sol-Gel Sci. Technol. 53 (2009) 162–170, https://doi.org/10.1007/s10971-009-2072-5.

[43] L. Yanyan, T.A. Kurniawan, Z. Ying, A.B. Albadarin, G. Walker, Enhanced photocatalytic degradation of acetaminophen from wastewater using WO3/TiO2/SiO2 composite under UV–VIS irradiation, J. Mol. Liq. 243 (2017) 761–770, https://doi.org/10.1016/j.molliq.2017.08.092.

[44] J. Peral, D. Ollis, Heterogeneous photocatalytic oxidation of gas-phase organics for air purification: acetone, 1-butanol, butyraldehyde, formaldehyde, and m-xylene oxidation, J. Catal. 136 (1992) 554–565, https://doi.org/10.1016/0021-9517(92)90085-v.

[45] M.-G. Jeong, E.J. Park, H.O. Seo, K.-D. Kim, Y.D. Kim, D.C. Lim, Humidity effect on photocatalytic activity of TiO2 and regeneration of deactivated photocatalysts, Appl. Surf. Sci. 271 (2013) 164–170, https://doi.org/10.1016/j.apsusc.2013.01.155.

[46] J. Shang, Y. Zhu, Y. Du, Z. Xu, Comparative studies on the deactivation and regeneration of TiO2 nanoparticles in three photocatalytic oxidation systems: C7H16, SO2, and C7H16–SO2, J. Solid State Chem. 166 (2002) 395–399, https://doi.org/10.1006/jssc.2002.9613.

[47] G. Odling, A. Ivaturi, E. Chatzisymeon, N. Robertson, Improving carbon-coated TiO2 films with a TiCl4 treatment for photocatalytic water purification, ChemCatChem 10 (2018) 234–243, https://doi.org/10.1002/cctc.201700867.
[48] J.O. Carneiro, V. Teixeira, S. Azevedo, F. Fernandes, J. Neves, Development of photocatalytic ceramic materials through the deposition of TiO_2 nanoparticles layers, J. Nano Res. (2012) 165–176, https://doi.org/10.4028/www.scientific.net/JNanoR.18-19.165.
[49] S.S. Al-Shamali, Photocatalytic degradation of methylene blue in the presence of TiO2 catalyst assisted solar radiation, Aust. J. Basic Appl. Sci. 7 (2013) 172–176.
[50] D.L. Cunha, A. Kuznetsov, C.A. Achete, A. Machado, M. Marques, Immobilized TiO2 on glass spheres applied to heterogeneous photocatalysis: photoactivity, leaching and regeneration process, PeerJ 6 (2018) e4464, https://doi.org/10.7717/peerj.4464.
[51] N. Abdullah, B.V. Ayodele, W.N. Wan Mansor, S. Abdullah, Effect of incorporating TiO2 photocatalyst in PVDF hollow fibre membrane for photo-assisted degradation of methylene blue, Bull. Chem. React. Eng. Catal. 13 (2018) 588, https://doi.org/10.9767/bcrec.13.3.2909.588-591.
[52] H.M. Ibrahim, Photocatalytic degradation of methylene blue and inactivation of pathogenic bacteria using silver nanoparticles modified titanium dioxide thin films, World J. Microbiol. Biotechnol. 31 (2015) 1049–1060, https://doi.org/10.1007/s11274-015-1855-9.
[53] H. Maleki, V. Bertola, TiO2 nanofilms on polymeric substrates for the photocatalytic degradation of methylene blue, ACS Appl. Nano Mater. 2 (2019) 7237–7244, https://doi.org/10.1021/acsanm.9b01723.